INTERNATIONAL JOURNAL FOR NUMERICAL METHODS IN FLUIDS
Int. J. Numer. Meth. Fluids **26**: 771–789 (1998)

AN EFFICIENT OPERATOR SPLITTING SCHEME FOR THREE-DIMENSIONAL HYDRODYNAMIC COMPUTATIONS

QIMIAO LU* AND ONYX W.H. WAI

Department of Civil and Structural Engineering, The Hong Kong Polytechnic University, Hung Hom, Kowloon, Hong Kong

SUMMARY

A new efficient numerical method for three-dimensional hydrodynamic computations is presented and discussed in this paper. The method is based on the operator splitting method and combined with Eulerian–Lagrangian method, finite element method and finite difference method. To increase the efficiency and stability of the numerical solutions, the operator splitting method is employed to partition the momentum equations into three parts, according to physical phenomena. A time step is divided into three time substeps. In the first substep, advection and Coriolis force are solved using the explicit Eulerian–Lagrangian method. In the second substep, horizontal diffusion is approximated by implicit FEM in each horizontal layer. In the last substep, the continuity equation is solved by implicit FEM, and vertical diffusion and pressure gradient are discretized by implicit FDM in each nodal column. The stability analysis shows that this method is unconditionally stable. A number of numerical experiments have been performed. The results simulated by the present scheme agree well with analytical solutions and the other documented model results. The method is efficient for 3D shallow water flow computations and fully fits complicated configurations. © 1998 John Wiley & Sons, Ltd.

KEY WORDS: three-dimensional numerical method; hybrid method; splitting method; Eulerian–Lagrangian method; shallow water equation; sigma co-ordinate transformation

1. INTRODUCTION

Only a few numerical methods for time-dependent, three-dimensional (3D), shallow water flow computations are known in current literature. These methods are commonly developed on the basis of finite difference method (FDM), finite element method (FEM), or the combination of both. The time schemes range from fully explicit to fully implicit. In general, FDM is more efficient and stable than FEM, but cannot fit complicated geometry. This may induce large errors in the simulations of hydraulic engineering problems with complex boundary configurations. Although FEM is suitable for arbitrary boundaries, its huge computer storage and computational time requirement, as well as poor stability, hinder its applications in 3D hydrodynamic modeling. A fully explicit scheme is highly efficient in computations, but imposes a severe limitation on time steps owing to the propagation of surface gravity waves. In contrast, a fully

* Correspondence to: Department of Civil and Structural Engineering, The Hong Kong Polytechnic University, Hung Hom, Kowloon, Hong Kong. Tel.: +852 2766025; Fax: +852 23346389; E-mail: 95980020r@hkpucc.polyu.edu.hk

CCC 0271–2091/98/070771–19$17.50

Received April 1996
Revised February 1997

implicit time scheme has good stability to allow a larger time step but the computations increase drastically because of its requirement of matrix inversion. For these reasons, the advancement of numerical methods in hydrodynamic computations has been turning to the direction of semi-implicit time schemes, combined with FEM and FDM.

In recent years, a few semi-implicit schemes and fully-implicit schemes with FDM or FEM have been developed for shallow water flows. Signorimi [1] employed an FEM in the horizontal planes coupling with FDM in the water column. Kawahara *et al.* [2] presented a multilayer finite element model with a lumped mass technique. Based on the multilayer system, a semi-implicit FEM with high-order shape functions was developed by Li and Zhan [3]. These FEMs transfer the 3D system into multiple two-dimensional (2D) horizontal systems which simplify the numerical formulations.

Benque *et al.* [4] developed a semi-implicit operator splitting method with an FDM for the simulations of 2D tidal flows. The governing equations were decomposed by the splitting method according to physical phenomena, then an FDM and a characteristic method were used for spatial discretization. Nicholson and O'Connor [5] developed a similar splitting method for 3D tidal flow and sediment transport computations. A fully implicit splitting method was developed by Wilders *et al.* [6] and extended to three dimensions by De Goede [7]. The methods described above were based on the ADI method [8] and improved ADI inaccuracies [4,9] in large time step. Other semi-implicit FDMs were presented by Casulli [10] and Casulli and Cheng [11]. In their schemes, the explicit Eulerian–Lagrangian method was used for the approximation of advection to linearize the momentum equations and simplify the solving system. Stability conditions of these schemes are free of the surface gravity wave propagation.

The study period of hydrodynamic investigations frequently stretches from days to seasons. It is essential for a surface water flow model to be equipped with an efficient, stable and accurate numerical algorithm for intensive and lengthy computations. An operator splitting formulation coupled with FEM and FDM is presented here for efficient computations of 3D shallow water currents. In the formulation, the governing equations are transformed into the sigma (σ) co-ordinate system. The computed domain is divided into multiple layers and each layer is meshed by finite elements. The splitting method is employed to partition the momentum equations into three parts according to the different physical significance, such as advection, horizontal diffusion and vertical diffusion. The advection is explicitly discretized by the Eulerian–Lagrangian method. The horizontal diffusion is discretized by the standard implicit Galerkin FEM, and the vertical diffusion is approximated by an implicit FDM for effi cient computations. This combination of numerical methods is not only efficient but also stable. The special grid arrangement is fitted to complex geometry and is also benefi cial to parallel computations. A number of numerical experiments are performed using this method. The computational efficiency, stability and accuracy of this method are illustrated in the numerical experiments.

2. THE GOVERNING EQUATIONS

The Navier–Stokes equations for shallow waters with the hydrostatic pressure assumption are transformed from Cartesian co-ordinates (x, y, z) to σ-co-ordinates (x_1, x_2, x_3) using the following expression

$$x_3 = \frac{z+h}{H}, \tag{1}$$

where h is the water depth relative to the mean sea level; $H = \zeta + h$ is the total water depth from the free surface to bottom; ζ is the water level (see Figure 1); and x_3 is the transformed vertical co-ordinate with the values of 0 at the bottom and 1 at the free surface. Using the chain rule and neglecting the higher-order hybrid derivatives, the governing equations in the σ-co-ordinate system can be derived as follows

$$\frac{\partial \zeta}{\partial t} + \frac{\partial H u_j}{\partial x_j} = 0, \tag{2}$$

$$\frac{\partial u_i}{\partial t} + u_j \frac{\partial u_i}{\partial x_j} + f\beta_{ij} u_j + g \frac{\partial \zeta}{\partial x_i} = \frac{\partial}{\partial x_j}\left(\varepsilon_j \frac{\partial u_i}{\partial x_j}\right), \tag{3}$$

where

$$u_j = \left\{u, v, \frac{1}{H}\left[w + (1 - x_3)u_i \frac{\partial\, h}{\partial x_i} - x_3\left(\frac{\partial \zeta}{\partial t} + u_i \frac{\partial \zeta}{\partial x_i}\right)\right]\right\};$$

$$\varepsilon_j = [\varepsilon_x, \varepsilon_y, \varepsilon_z H^{-2}]; \qquad x_j = [x, y, (z+h)H^{-1}];$$

$$\beta_{ij} = \begin{bmatrix} 0 & -1 & 0 \\ 1 & 0 & 0 \end{bmatrix}; \qquad i = 1, 2; \qquad j = 1,\ldots,3;$$

u, v and w are components of velocity in the x-, y- and z-directions, respectively; ε_x, ε_y and ε_z are eddy diffusion coefficients of water in the x-, y- and z-directions, respectively (see Figure 1); t is time; f is the Coriolis parameter ($f = 2\omega \sin\theta$); ω is the angular frequency of the earth rotation; θ is the latitude of the computed region. In Equations (2) and (3), the vertical co-ordinate is linearly transformed into uniform co-ordinate, which simplifies the numerical formulations.

3. OPERATOR SPLITTING

The shallow water momentum equations account for the fluid advection, horizontal and vertical diffusions, Coriolis force and pressure variation. The characteristic temporal and spatial scales associated with these hydraulic phenomena span several orders of magnitude. Thus, each mathematical term in the momentum equations carries a certain amount of physical and numerical significance in a hydrodynamic model. For instance, the pressure

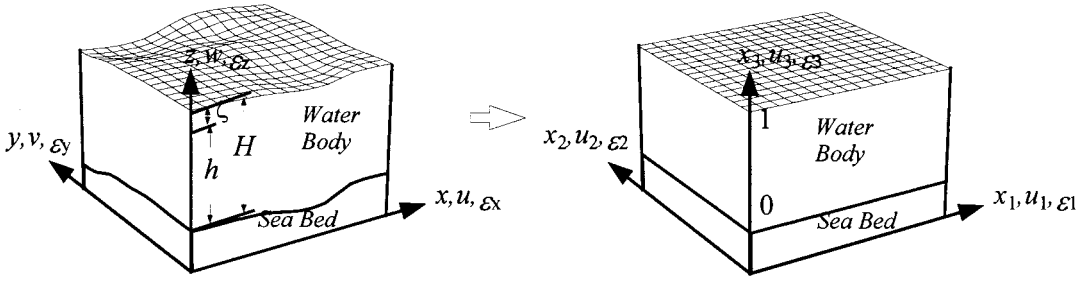

Figure 1. Definition of variables and σ-transformation in the 3D model.

gradient terms are principally responsible for the general movement of water. The vertical diffusion terms are key elements in a 3D model. The non-linearity of the advection terms easily causes numerical instability. Contrarily, the horizontal diffusion terms take a smoothing effect that creates a more stable numerical environment. It is more correct to treat these terms with suitable numerical methods according to their particular physical and numerical natures.

In this model, the time integration of the momentum equations in a time step is partitioned into three sequential substeps. So a simpler system conforming to a particular physical characteristic, decomposed from the complicated momentum equations, is involved in a substep. The continuity equation, however, is integrated in a time step for the purpose of mass conservation.

In the first substep, the system constituting the advection and Coriolis force terms is solved for the velocity. In general, numerical instability in hydrodynamic computations is mainly caused by the incorrect approximation of the advection terms. To improve the numerical stability, the advection terms in this system are discretized at an integer time step (e.g. $n\Delta t$, where Δt is the time step). The equation in this substep is given as

$$\frac{u_i^{n+1/3} - u_i^n}{\Delta t} + u_j \frac{\partial u_i}{\partial x_j} + f\beta_{ij} u_j = 0, \quad i = 1, 2, 3; \quad j = 1, 2, 3. \tag{4}$$

In the second substep, only the horizontal diffusion terms are considered, as follows:

$$\frac{u_i^{n+2/3} - u_i^{n+1/3}}{\Delta t} = \frac{\partial}{\partial x_j}\left(\varepsilon_j \frac{\partial u_i}{\partial x_j}\right), \quad i, j = 1, 2. \tag{5}$$

Shallow water flows with free surfaces are principally driven by pressure gradients and/or surface shear stresses such as wind, but obstructed by bottom friction. The surface shear stresses and the bottom friction are essentially associated with the vertical diffusion in a 3D model. Therefore, the pressure gradient and vertical diffusion terms are grouped together to determine the velocity in the last substep, as shown below.

$$\frac{u_i^{n+1} - u_i^{n+2/3}}{\Delta t} + g \frac{\partial \zeta}{\partial x_i} = \frac{\partial}{\partial x_3}\left(\varepsilon_3 \frac{\partial u_i}{\partial x_3}\right), \quad i = 1, 2. \tag{6}$$

To ensure mass equilibrium in an element, the continuity equation is integrated in a time step to solve the surface elevation. By integrating Equation (2) from the bottom to surface with the following boundary conditions

$$\begin{cases} w|_{z=\zeta} = \dfrac{\partial \zeta}{\partial t} + u_j|_{z=\zeta} \dfrac{\partial \zeta}{\partial t} & \text{at the surface} \\ w|_{z=-h} = -u_j|_{z=-h} \dfrac{\partial h}{\partial x_j} & \text{at the bottom,} \end{cases} \tag{7}$$

i.e. $u_3 = 0$ at the water surface ($x_3 = 1$) as well as at the bottom ($x_3 = 0$), the continuity equation becomes

$$\frac{\partial \zeta}{\partial t} + \frac{\partial\ HQ_j}{\partial x_j} = 0, \tag{8}$$

where $Q_j = \int_0^1 u_j \, \mathrm{d}x_3$, $j = 1, 2$ is the vertical averaged velocity in the x_j-direction.

The differential equation for solving the vertical velocity is given in Equation (9), which is also obtained from the continuity equation.

$$Hu_3 + \frac{\partial \zeta}{\partial t} x_3 + \frac{\partial Hq_j}{\partial x_j} = 0, \tag{9}$$

where $q_j = \int_0^{x_3} u_j \, \mathrm{d}x_3$, $j = 1, 2$.

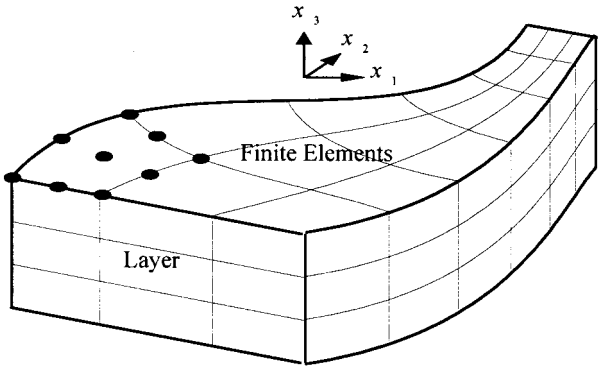

Figure 2. Grid arrangement in σ-co-ordinate system.

4. SPATIAL DISCRETIZATION

The spatial discretization and the nodal arrangement for the above mentioned differential equations are described in this section. Because of the σ-co-ordinate transformation, the computing domain is transformed into a uniform depth domain in which the governing equations are discretized and solved. Thus, the nodes can be uniformly arranged in the vertical direction, i.e. the transformed domain is divided into a number of horizontal layers with equal thickness. In each horizontal layer, the finite elements are used to fit complex geometry (see Figure 2).

For accurate computations, the nine-node isoparameteric quadrilateral finite elements are employed. According to Thomasset [12], the spatial gradient of the velocity is one order higher than that of the surface elevation. Therefore, the basic shape function selected for velocities is a two-order polynomial function while a one-order polynomial function is used for the surface elevation and water depth in a finite element [13], i.e.

$$\begin{cases} u = u_{i,j}\phi_j \\ \zeta = \zeta_j\varphi_j, \quad h = h_j\varphi_j \end{cases}, \quad j = 1,\ldots,9, \tag{10}$$

where the subscript j denotes the jth node, and ϕ and φ are the two- and one-order polynomial functions, respectively.

4.1. Approximation of advection with Eulerian–Lagrangian method

In the first substep, Equation (4) is solved for the velocity $u_i^{n+1/3}$. The advection non-linearity in Equation (4) causes the difficulty of numerical discretization and instability. Eulerian–Lagrangian methods are able to linearize the non-linear advection terms along the streamline with the acceptable stability. Casulli's investigations [10,11] have shown that the Eulerian–Lagrangian approximation was relatively accurate and unconditionally stable for the advection terms. The Eulerian–Lagrangian methods, similar to the upwind method and characteristic methods, are more physically sound than other methods in the aspect of the advective physical behavior. For this reason, an explicit Eulerian–Lagrangian scheme is employed for the advection terms in this model. The Coriolis force terms are implicitly approximated for the purpose of stability [14]. Therefore, Equation (4) can be rewritten as follows:

$$\frac{u_i^{n+1/3}-u_i^n}{\Delta t}+u_j^n\frac{\partial u_i^n}{\partial x_j}+f\beta_{ij}u_j^{n+1/3}=0, \quad i=1,2, \quad j=1,2,3. \tag{11}$$

To obtain the Eulerian–Lagrangian approximation, a streamline which is the displacement of a particle passing from the point x_i over time is defined as follows:

$$\frac{\mathrm{d}x_i}{\mathrm{d}t}=u_i^n, \quad i=1,2,3. \tag{12}$$

Along the streamline, the co-ordinate of point p, which is being convected to the point x_i in a lapsed time Δt (see Figure 3), can be derived from Equation (12).

$$x_{i,p}=x_i-\Delta t u_i^n, \quad i=1,2,3.$$

Note that $u_{i,p}^n$ is the velocity of the point p at time $n\Delta t$ in the x_i -direction. The following approximate expression is obtained using the Taylor expansion.

$$u_{i,p}^n\approx u_i^n-\Delta t u_j^n\frac{\partial u_i^n}{\partial x_j}, \quad i=1,2; \quad j=1,2, \ 3.$$

Thus, the solution of Equation (11) at the grid point x_i can be obtained directly from the following equation:

$$u_i^{n+1/3}=A_{ij}u_{j,p}^n, \quad i,j=1,2, \tag{13}$$

where

$$A_{ij}=\frac{1}{1+(\Delta tf)^2}\begin{bmatrix}1 & \Delta tf\\ -\Delta tf & 1\end{bmatrix}.$$

In fact, the streamline described in Equation (12) is not a straight line over time Δt because the velocity u_i is not constant along the streamline. For large time steps, using direct integration of Equation (12) to calculate the co-ordinates of p may cause a large computation error, or result in the streamline passing through the solid boundary. For this reason, the time step Δt is divided into K equal time pieces of length $\delta t=\Delta t/K$. By integrating Equation (12), the streamline is traced backwards from the point x_i over time Δt with the following iteration:

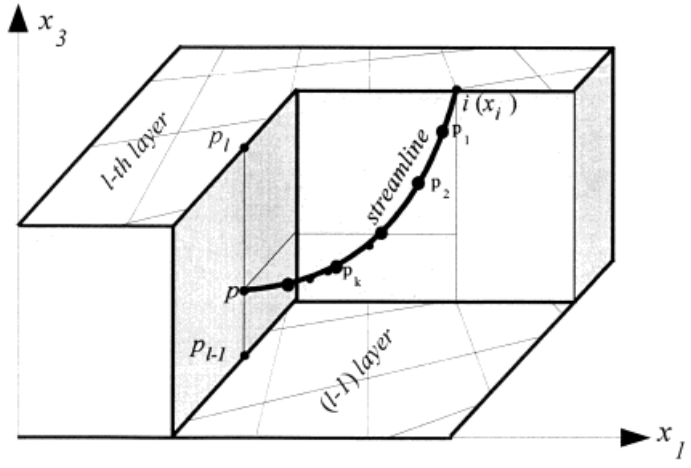

Figure 3. Definition of a streamline passing through point x_i.

$$\begin{cases} x_{i,0} = x_i, \qquad u_{i,0} = u_i(x_i) \\ x_{i,k} = x_{i,k-1} - u_{i,k-1}\delta t, \qquad u_{i,k-1} = u_i(x_{i,k}), \quad k = 1,\ldots,K; \quad i = 1, 2, 3, \\ x_{i,p} = x_{i,K} \end{cases} \tag{14}$$

where $x_{i,k}$ is the co-ordinate of the point p_k obtained after the kth iteration (see Figure 3), $u_{i,k}$ is the velocity at p_k. In practice, the point p_k may not be located at a grid point and/or a layer. So the vertical bilinear interpolation should be used to calculate $u_{i,k}$ as follows:

$$u_{i,k} = \begin{cases} \frac{1}{2}\alpha(1+\alpha)u_{i,k}^{(l-1)} + (1-\alpha^2)u_{i,k}^{(l)} - \frac{1}{2}\alpha(1-\alpha)u_{i,k}^{(l+1)} & \text{for } \alpha \le 0.5 \\ -\frac{1}{2}\alpha(1-\alpha)u_{i,k}^{(l-2)} + \alpha(2-\alpha)u_{i,k}^{(l-1)} + \frac{1}{2}(1-\alpha)(2-\alpha)u_{i,k}^{(l)} & \text{for } \alpha > 0.5 \end{cases}$$

Here, $u_{i,k}^{(l)}$ is the velocity at the projecting point of p_k on the lth layer, calculated by Equation (10); $x_3^{(l)} > x_{3,k} > x_3^{(l-1)}$; $\alpha = (x_3^{(l)} - x_{3,k})/\Delta\sigma$; $\Delta\sigma = x_3^{(l)} - x_3^{(l-1)}$, is the thickness of a layer.

4.2. Approximation of horizontal diffusion with implicit FEM

In the second substep, Equation (5) is approximated by the implicit FEM in each layer as follows:

$$\mathbf{D}\mathbf{u}_i^{n+2/3} = \mathbf{M}\mathbf{u}_i^{n+1/3}, \tag{15}$$

where $\mathbf{u}_i = [u_{i,1}, u_{i,2}, \ldots, u_{i,N}]^T$, and N is the number of nodes in a layer,

$$D_{jk} = M_{jk} + \Delta t \varepsilon_i F_{jk}, \qquad M_{jk} = \int_\Omega \phi_j \phi_k \, d\Omega,$$

$$F_{jk} = \int_\Omega \frac{\partial \phi_j}{\partial x_i}\frac{\partial \phi_k}{\partial x_i} \, d\Omega - \oint_\Gamma \frac{\partial \phi_k}{\partial n}\phi_j \, d\Gamma, \quad i = 1, 2; \quad j, k = 1,\ldots,N.$$

Γ is the boundary around the interested domain Ω and $\partial/\partial n$ is the derivative normal to the boundary. For fixed grids and constant horizontal eddy coefficients, the matrix $\mathbf{D}$ becomes a constant coefficient matrix in all layers over the entire computation period. The inverse of matrix $\mathbf{D}$ can be calculated in advance, thus, it will greatly save the computational time. And also, this scheme is beneficial for parallel computations because of the convenient vectorization.

4.3. Approximation of continuity equation with implicit FEM, pressure gradient and vertical diffusion with implicit FDM

In the last substep, the continuity equation (8), and the vertical diffusion and pressure gradient terms in the momentum equation (6) are used to solve for the surface elevation and velocities. To ensure mass conservation in an element and obtain stable and efficient computations, the continuity equation is discretized by the fully implicit FEM, while the momentum equation is approximated by the fully implicit FDM. However, the computation efficiency is reduced if the two equations are solved simultaneously. For this reason, in the continuity equation, Q_i^{n+1} should be eliminated by Equation (6). By integrating Equation (6) from the bottom to surface with the following boundary conditions,

$$\begin{aligned} \varepsilon_3 \left.\frac{\partial u_i}{\partial x_3}\right|_{x_3=1} &= \frac{\tau_i^w}{H} && \text{at bottom} \\ \varepsilon_3 \left.\frac{\partial u_i}{\partial x_3}\right|_{x_3=0} &= \frac{\tau_i^b}{H} = \frac{g u_{i,1}^{n+2/3}\sqrt{u_{j,1}^{n+2/3}u_{j,1}^{n+2/3}}}{C^2 H} && \text{at surface} \end{aligned} \quad , \quad i, j = 1, 2,$$

the continuity equation becomes the following form:

$$\frac{\zeta^{n+1}-\zeta^n}{\Delta t}+\frac{\partial(Q_i^{n+2/3}H^{n+1})}{\partial x_i}-\Delta t g\frac{\partial}{\partial x_i}\left(H^{n+1}\frac{\partial\zeta^{n+1}}{\partial x_i}\right)+\Delta t\frac{\partial}{\partial x_i}(\tau_i^w-\tau_i^b)=0. \tag{16}$$

Here, $i=1$, 2, and τ_i^w, τ_i^b are the components of the surface and bottom shear stresses in the x_i-direction, respectively. Thus, the above differential equation can be independently solved in the horizontal plane (the x_1–x_2 plane). Applying the standard Galerkin method gives

$$\mathbf{G}\zeta^{n+1}=\mathbf{Z}, \tag{17}$$

where

$$G_{jk}=J_{jk}-\Delta tE_{jk}+\Delta t^2gS_{jkl}H_l,$$

$$Z_j=J_{jk}\zeta_k^n+\Delta tE_{jk}h_k-\Delta t^2T_{i,\,jk}(\tau_{i,k}^w-\tau_{i,k}^b),$$

$$J_{jk}=\int_\Omega\varphi_k\phi_j\,\mathrm{d}\Omega;\qquad T_{i,\,jk}=\int_\Omega\frac{\partial\phi_k}{\partial x_i}\phi_j\,\mathrm{d}\Omega,$$

$$E_{jk}=\int_\Omega Q_i^{n+2/3}\varphi_k\frac{\partial\phi_j}{\partial x_i}\,\mathrm{d}\Omega-\oint_\Gamma Q_n^{n+2/3}\varphi_k\phi_j\,\mathrm{d}\Gamma,$$

$$S_{jkl}=\int_\Omega\varphi_l\frac{\partial\varphi_k}{\partial x_i}\frac{\partial\phi_j}{\partial x_i}\,\mathrm{d}\Omega-\oint_\Gamma\frac{\partial\varphi_k}{\partial n}\phi_j\,\mathrm{d}\Gamma,\quad i,j,k=1,\ldots,N.$$

Q_n is the vertical averaged velocity normal to the boundary. Because Equation (17) is a set of non-linear algebraic equations, an iteration method must be used to obtain the solutions.

Now an implicit FDM is used to discretize Equation (6) in each vertical grid column. With the central difference scheme and insertion of the boundary conditions at the bottom and surface, the finite difference approximation of Equation (6) is found to be

$$\mathbf{B}\mathbf{u}_i^{n+1}=\mathbf{V}_i, \tag{18}$$

where $\mathbf{u}=[u_{i,1},u_{i,2},\ldots,u_{i,L}]^T$, $u_{i,1}$ is the velocity at the lth layer, L is the number of vertical layers, $\mathbf{B}$ is a triangular coefficient matrix and $\mathbf{V}_i$ is a known vector defined as

$$B_{1,1}=1+2\delta(\lambda_{3/2}+g\sqrt{u_{j,1}^{n+2/3}u_{j,1}^{n+2/3}}/C^2H),\qquad B_{1,2}=-2\delta\lambda_{3/2},$$

$$B_{k,k-1}=-\delta\lambda_{k-1/2},\qquad B_{k,k}=1+\delta(\lambda_{k-1/2}+\lambda_{k+1/2}),\qquad B_{k,k+1}=-\delta\lambda_{k+1/2},$$
$$k=2,\ldots,L-1,$$

$$B_{L,L-1}=-2\delta\lambda_{L-1/2},\qquad B_{L,L}=1+2\delta\lambda_{L-1/2},$$

$$\delta=\frac{\Delta t}{\Delta\sigma},\qquad \lambda_{k+1/2}=\frac{\varepsilon_{3,k}+\varepsilon_{3,k+1}}{2\Delta\sigma},$$

$$V_{i,k}=u_{i,k}^{n+2/3}-g\Delta t\frac{\partial\zeta^{n+1}}{\partial x_i},\qquad k=1,\ldots L-1,$$

$$V_{i,L}=u_{i,L}^{n+2/3}-g\Delta t\frac{\partial\zeta^{n+1}}{\partial x_i}+2\delta\tau_i^w/H.$$

The surface elevation derivative can be easily calculated using Equation (10) as shown below.

$$\left(\frac{\partial\zeta^{n+1}}{\partial x_i}\right)_j=\frac{1}{m_j}\sum_{e=1}^{m_j}\left(\frac{\partial\varphi_k^{(e)}}{\partial x_i}\right)_j\zeta_k$$

where $\varphi^{(e)}$ denotes the shape function in the eth element, m_j is the number of elements around the jth node. Evidently, the algebraic Equation (18) can be solved efficiently by the double sweep method and easily transformed to parallel computation algorithms.

The vertical velocity can be directly solved from Equation (9) as follows:

$$u_{3,j}^{n+1} = -\frac{1}{H_j^{n+1}}\left[\frac{\zeta_j^{n+1}-\zeta_j^n}{\Delta t}x_3 + \left(\frac{\partial(Hq_i^{n+1})}{\partial x_i}\right)_j\right], \tag{19}$$

where

$$\left(\frac{\partial(Hq_i^{n+1})}{\partial x_i}\right)_j = \frac{1}{m_j}\sum_{e=1}^{m_j}\left(\frac{\partial(\phi_l^{(e)}\varphi_k^{(e)})}{\partial x_i}\right)_j q_{i,l}^{n+1}H_k^{n+1}.$$

Equation (19) is efficiently solved without any matrix inversion involved and easily applied to parallel computations.

5. STABILITY AND EFFICIENCY

The stability of the proposed scheme is analyzed by the von Neumann method. For simplicity, the stability of the scheme is respectively studied in the three substeps. At first, a harmonic decomposition error at the time $n\Delta t$ is introduced as shown below.

$$E^n = \xi^n e^{i\gamma_j x_j}, \quad j = 1, 2, 3, \tag{20}$$

where ξ is an error amplification factor, γ_i is a frequency of the error in the x_i-direction, i is the complex number $\sqrt{-1}$. By replacing u_i in Equation (13) with Equation (20), the error amplification factor in the first substep is obtained as follows:

$$\left|\frac{\xi^{n+1/3}}{\xi^n}\right| = \left|Ae^{i\gamma_j\Delta x_{j,p}}\right| = \|A\| = 1, \quad j = 1, 2, 3. \tag{21}$$

Here, $\Delta x_{j,p} = x_j - x_{j,p}$. It can be seen that the approximation of Equation (13) is unconditionally stable.

By introducing an error in the finite element approximation of Equation (15), the error amplification factor in the second substep is derived as

$$\left|\frac{\xi^{n+2/3}}{\xi^{n+1/3}}\right| = |\mathbf{D}^{-1}\mathbf{M}| = \frac{|\mathbf{M}|}{|\mathbf{M}+\Delta t\varepsilon\mathbf{F}|}. \tag{22}$$

Both the mass matrix $\mathbf{M}$ and the stiffness matrix $\mathbf{F}$ are positive-definite, therefore, there exists an invertible matrix $\mathbf{P}$ such that $\mathbf{P}^T\mathbf{M}\mathbf{P} = \mathbf{I}$, in which $\mathbf{I}$ is the identity matrix and the superscript T denotes the transpose of the matrix. The congruent matrix $\mathbf{F}_1 = \mathbf{P}^T\mathbf{F}\mathbf{P}$ is also positive-definite and symmetric. Therefore, an orthogonal matrix Λ can be found to diagonalize $\mathbf{F}_1$, i.e.

$$\Lambda^T\mathbf{F}_1\Lambda = \Lambda^T\mathbf{P}^T\mathbf{F}\mathbf{P}\Lambda = \mathrm{diag}\,(\chi_1, \chi_2, \ldots, \chi_N),$$

where, $\chi_1, \chi_2, \ldots, \chi_N$ are the eigenvalues of $\mathbf{F}_1$ and $\chi_i > 0$, $i = 1, 2, \ldots, N$. Using the characteristic of the orthogonal matrix $\Lambda^T\Lambda = \mathbf{I}$, the following determinant is obtained

$$|\mathbf{P}^T||\mathbf{M}+\Delta t\varepsilon\mathbf{F}||\mathbf{P}| = |\mathbf{I}+\Delta t\varepsilon\mathbf{F}_1| = |\Lambda^T||\mathbf{I}+\Delta t\varepsilon\mathbf{F}_1||\Lambda| = \prod_{i=1}^{N}(1+\Delta t\varepsilon\chi_i) \geq 1$$

Thus,

$$|\mathbf{M}+\Delta t\varepsilon\mathbf{F}| \geq |\mathbf{P}^T|^{-1}|\mathbf{P}|^{-1} = |(\mathbf{P}^T)^{-1}\mathbf{P}^{-1}| = |\mathbf{M}|. \tag{23}$$

From the above inequality, the amplification factor in the second substep is always ≤ 1, such that the finite element approximation, Equation (15), is unconditionally stable.

Similarly, the error amplification of the finite difference approximation, Equation (18), in the last substep can be derived as

$$\left|\frac{\xi^{n+1}}{\xi^{n+2/3}}\right| = \left|1 + \frac{4\Delta t}{\Delta\sigma^2}\,\varepsilon_3 \sin^2\frac{\gamma_3\Delta\sigma}{2} + i\,\frac{\Delta t g}{2\Delta x_j}\sin\gamma_j\Delta x_j\right|^{-1} \le 1, \quad j = 1 \text{ or } 2. \tag{24}$$

Undoubtedly, the approximation of Equation (18) is also unconditionally stable. Thus, the error amplification factor over a time step is given as

$$|\xi| = \left|\frac{\xi^{n+1}}{\xi^n}\right| = \left|\frac{\xi^{n+1/3}}{\xi^n}\right| \cdot \left|\frac{\xi^{n+2/3}}{\xi^{n+1/3}}\right| \cdot \left|\frac{\xi^{n+1}}{\xi^{n+2/3}}\right| \le 1. \tag{25}$$

Hence, the present scheme for the momentum equations is proven to be unconditionally stable.

In the stability analysis of Equation (17), the velocity $Q_i^{n+2/3}$ and the water depth H^{n+1} are assumed to be constants, due to the difficulty of stability analysis for non-linear algebraic equations. For simplicity, the following one-dimensional form of Equation (16) is used to analyze the stability because the numerical behaviors of Equation (16) are consistent in the x_1- and x_2-directions.

$$\frac{\zeta^{n+1} - \zeta^n}{\Delta t} + Q\frac{\partial\zeta}{\partial x} - \Delta t g H\frac{\partial^2\zeta}{\partial x^2} = 0. \tag{26}$$

Thus, for the typical node i, the assembled implicit finite element equations can be obtained as follows [15].

$$\frac{(\zeta_{i-1}^{n+1} + 4\zeta_i^{n+1} + \zeta_{i+1}^{n+1}) - (\zeta_{i-1}^n + 4\zeta_i^n + \zeta_{i+1}^n)}{6\Delta t} + Q\frac{\zeta_{i+1}^{n+1} - \zeta_{i-1}^{n+1}}{2\Delta x} - \Delta t g H\frac{\zeta_{i-1}^{n+1} + 2\zeta_i^{n+1} + \zeta_{i+1}^{n+1}}{\Delta x^2} = 0.$$

By introducing the error of Eq. (20), the amplification factor of the above algebraic equation is obtained.

$$|\xi| = \left|\frac{\xi^{n+1}}{\xi^n}\right| = \left|\frac{3 - 2\sin^2(\frac{1}{2}\gamma\Delta x)}{3 - (2 - 12gH\Delta t^2/\Delta x^2)\sin^2(\frac{1}{2}\gamma\Delta x) + i(3Q\Delta t/\Delta x)\sin(\gamma\Delta x)}\right| \le 1.$$

Obviously, the fully implicit finite element scheme of Equation (26) is unconditionally stable. Extending it to two dimensions, it can be proven that the fully implicit finite element scheme for a two-dimensional advection-diffusion equation such as Equation (16) is still unconditionally stable. Therefore, the present implicit finite element scheme of Equation (17) is unconditionally stable.

To verify the stability of the present scheme in actual simulations, a test case is set up to simulate a steady flow in a rectangular channel. The flow is induced by the water level difference of 2 mm between the inflow and outflow. The channel dimension is 1000 m wide, 2000 m long and 10 m deep. The water body is divided into 11 vertical layers and 50 square finite elements of 231 nodes with grid size 100 m in each horizontal layer. The simulations are performed with time steps varied from 600 to 9000 s, corresponding to the Courant numbers of 9–135. The surface velocities at the channel center simulated with these time steps are shown in Figure 4. It can be seen that the simulations are completely stable, despite the slight numerical oscillations at the beginning of the flow development in the large time step simulations. In fact, these numerical oscillations are induced by the first-order time accuracy, $o(\Delta t)$, rather than by the scheme stability.

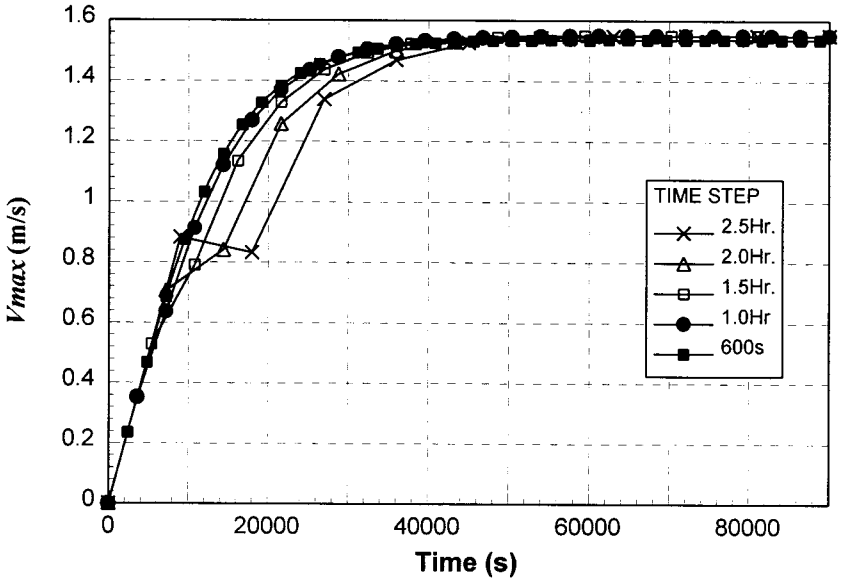

Figure 4. Stability test of a channel flow.

The computation efficiency is investigated in the test case. The computation is performed using PC Pentium-120 Mhz. The total memory required for the computation is ≈ 2.0 Mbytes. The computational time at each time step is listed in Table 1. It can be seen that the present combined scheme is very efficient for the diffusion computations in the last two steps. The computation in the first substep, which depends on the iterative number K (see Section 4.1, $K = 10$ in the test case), takes slightly longer than in the other substeps. To illustrate the present scheme efficiency, it is necessary to compare the method with the other 3D method. For the case of the 3D semi-implicit multilayer model, the computational amount for the momentum equations at each time step is as much as $2L$ times for an advective-diffusion equation. The running time for this test case with the above multilayer method is estimated to be 4235 (s/100). This figure shows that the present scheme is ≈ 20 times faster than the multilayer model in the momentum computations. Furthermore, the computation efficiency will increase much more if this scheme is applied to mass transport models such as the sediment transport model and water quality model.

The computational time for the continuity equation depends on the iterative convergence of Equation (17). In general, the iterative convergence is fast in shallow water flow simulations because the variation of surface elevation is much less than the water depth. For example, the

Table 1. The computational time at each time step

Substep	Computational time (s/100)			
Equations	In 1st substep	In 2nd substep	In 3rd substep	Total
Momentum equations	153	49	2	204
Continuity equation	–	–	385	335
Vertical velocity	–	–	50	50
Total	153	49	437	639

iterative number in the test case is less than three under the given precision, 10^{-6}. The results show that the present scheme is highly efficient for the shallow water flow computations.

6. MODEL VERIFICATION

To verify the applicability of the present numerical scheme, four numerical experiments are performed. These numerical experiments are also used to present the physical behaviors of the different terms such as advection, Coriolis force, horizontal diffusion, etc. in the general flow patterns. The simulated results will be compared with both the analytic solutions and the numerical results computed by other documented models in this section.

6.1. Wind-driven flow in a rectangular channel

This numerical experiment is designed to verify velocity profiles in the 3D flow field by simulating a wind-driven flow in a rectangular channel. The dimension of the channel is 2000 m in length, 1000 m wide and 10 m deep. The water body is divided into 11 layers, and each layer is decomposed by 50 finite elements with grid size 100×100 m and 231 nodes. The free surface is subject to a constant longitudinal wind induced stress of $\tau_1^w = 1.5$ Nm^{-2} and $\tau_2^w = 0$ Nm^{-2}. The no-slip condition is imposed on the bottom and the horizontal diffusion and Coriolis forces are neglected in the experiment. The flow parameters of

$$\varepsilon_z = 0.010 \text{ m}^2 \text{ s}^{-1}, \qquad \rho = 1025 \text{ kg m}^{-3},$$

and the large time step of 600 s are employed in the simulation.

The computed steady velocity profile at the center of the channel is compared with the corresponding analytical solution [16] (see Figure 5). It can be seen that the numerical simulated result agrees quite well with the analytical solution.

6.2. Wind-driven flow with Coriolis force in a deep basin

This numerical experiment is to simulate the flow driven by wind and affected by Coriolis force in a deep rectangular basin. The basin represents the North Sea with dimensions of north–south length of 800 km, west–east length of 400 km and uniform depth of 65 m as considered by Davies [14] and Li [3]. The water body is divided into 11 layers, in which 32 finite elements with grid size 50×50 km and 153 nodes are arranged. The water, initially at rest, is subject to a uniform northerly wind stress of $\tau_1^w = 0$ Nm^{-2} and $\tau_2^w = -1.5$ Nm^{-2}. Referring to the other documented models, the flow parameters are set as

$$\varepsilon_x = \varepsilon_y = 0 \text{ m}^2 \text{ s}^{-1}, \qquad \varepsilon_z = 0.065 \text{ m}^2 \text{ s}^{-1}, \qquad f = 0.44 \text{ hr}^{-1}, \qquad \rho = 1025 \text{ kg m}^{-3},$$

$$C = 13 \text{ m}^{0.5} \text{ s}^{-1}.$$

A time step of 1800 s is used in the 5 day continuous simulation.

The computed steady state velocity profiles at the basin center are compared with Davis' and Li's results (see Figure 6). It can be seen that the present solutions agree well with the other two sets of numerical results. The time series of the surface velocity at the basin center is shown in Figure 7. The flow oscillations simulated by the present model are revealed in

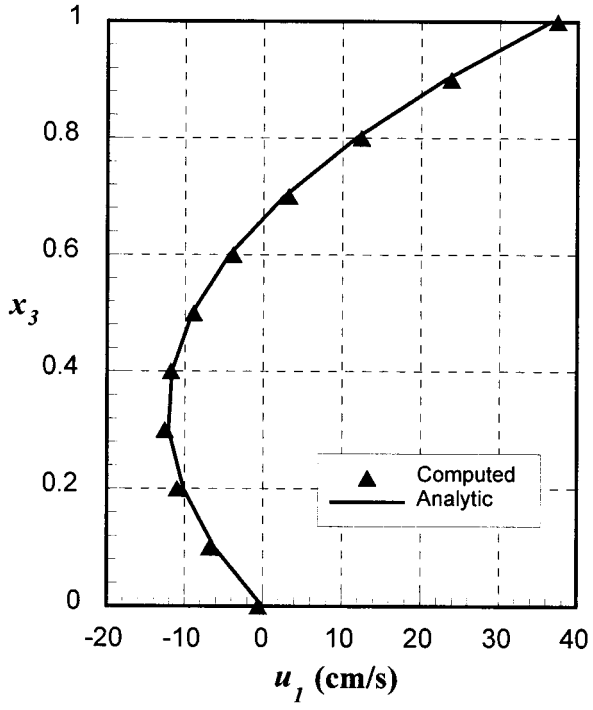

Figure 5. Comparison of the computed and analytic velocity profiles in a wind-driven flow.

Figure 8. From these figures, the flow oscillation development can be described as two stages. In the first stage, the slope of water level in the north–south direction increases with the development of the surface flow, subject to the wind stress. When the force induced by the adverse pressure gradient is equal to the wind induced force, the flow turns to the second stage. In this stage, the opposite flow near the bottom develops with increasing magnitude, while the surface flow reduces its intensity due to the energy transfer, exchange and dissipation through vertical diffusion between the surface and bottom boundary layers. Both of these stages alternate several times until the steady flow is reached.

6.3. Vertical recirculating flow in a dredged channel

Vertical flow recirculation often takes place in sharp topographic areas such as dredged ditches. This numerical experiment is to simulate vertical recirculating flows in a dredged ditch perpendicular to the flow direction. The simulating domain is an open rectangular channel with dimensions of length 800 m, width 400 m and depth 10 m. In the channel, an artificial ditch is dredged with depth 16.5 m and width 200 m (see Figure 9). A constant flow is produced by setting the two end boundaries with water levels of ± 2 mm. The water body is divided into 80 finite elements and 369 nodes in each of the 21 layers. The grids are refined in the dredged ditch area for an accurate simulation of vertical recirculation. In the simulation, a parabolic-constant distribution of the vertical diffusive coefficient is employed as shown below.

$$\varepsilon_z = \begin{cases} ku_* H x_3(1-x_3) & \text{for } x_3 < 0.5 \\ 0.25\kappa u_* H & \text{for } x_3 \geq 0.5 \end{cases},$$

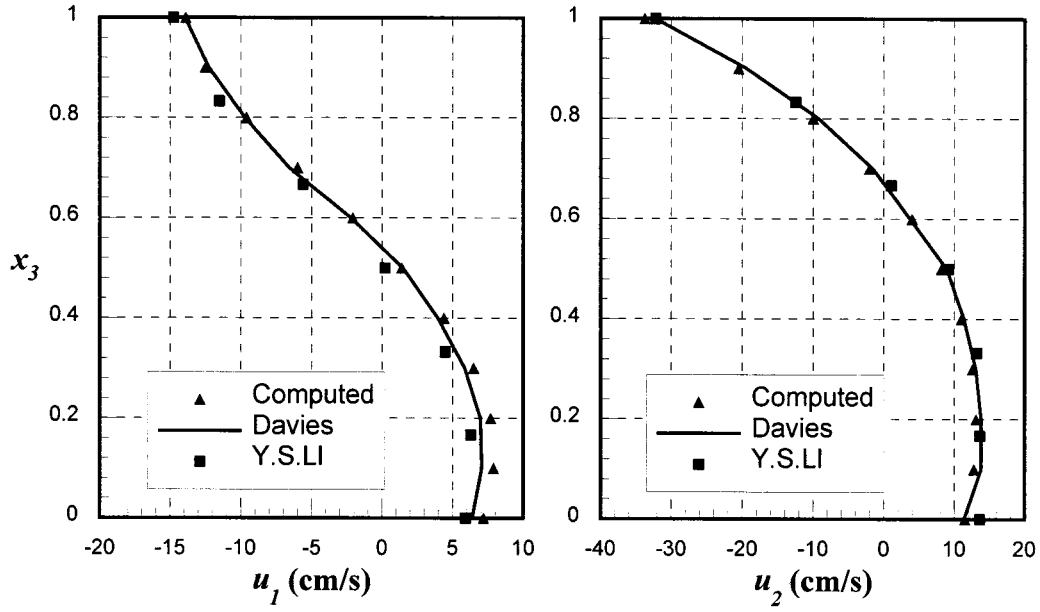

Figure 6. Comparison of the computed velocity profiles at the basin center with other documented models.

where κ is the von Karman constant equal to 0.4, u_* is a current-related bed shear velocity. The other flow parameters are set as

$$\varepsilon_x = \varepsilon_y = 1.0 \text{ m}^2 \text{ s}^{-1}, \qquad f = 0 \text{ hr}^{-1}, \qquad \rho = 1025 \text{ kg m}^{-3}, \qquad C = 60 \text{ m}^{0.5} \text{ s}^{-1}.$$

The time step of 120 s is used in the simulation.

The initial vertical recirculation development in the dredged ditch on the x–z plane is shown in Figure 10 (u–w vector plot). It can be seen that a small recirculation appears, firstly at the lower upstream corner of the ditch. Then, the recirculation expands and moves downstream with time. When the first recirculation reaches the downstream corner of the ditch, another, more profound, second recirculation develops at the upstream corner. The first recirculation is replaced by the second fully developed downstream-moving recirculation. This alternate recirculating pattern repeats once every 30 min (see Figure 11). The numerical results reveal

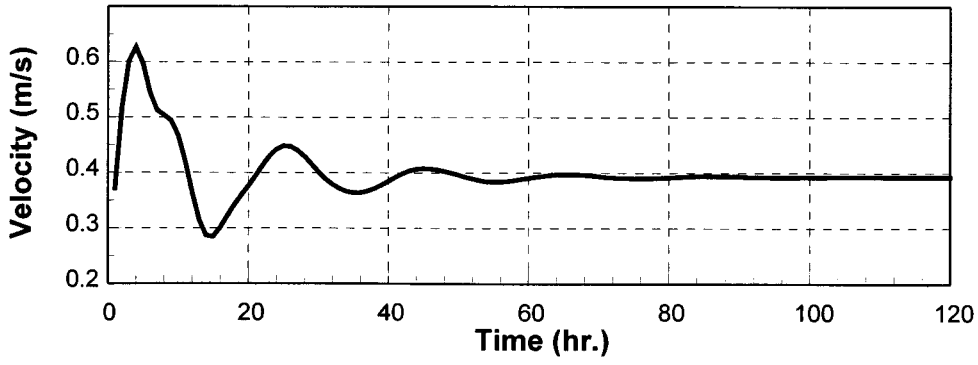

Figure 7. Time series of surface velocity at the basin center.

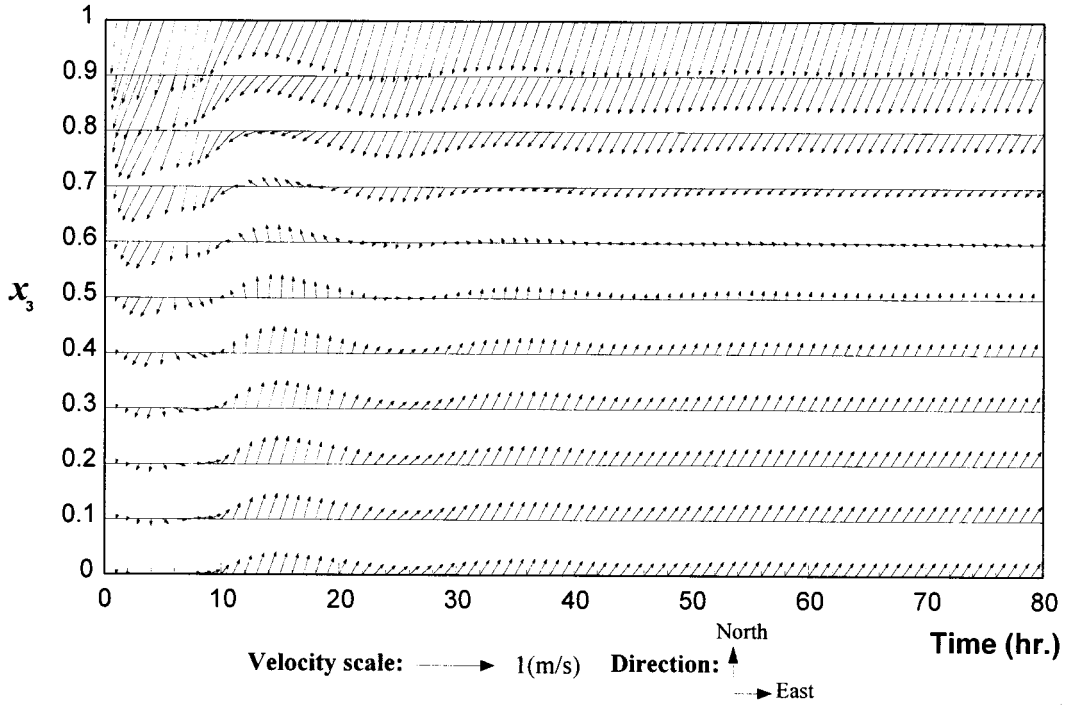

Figure 8. Time series of the velocity vectors at the basin center in the water column.

a reasonable physical recirculation pattern. The appearance of the two alternate recirculation modes depends on the inflow velocity and the geometry of the dredged channel.

6.4. Development of eddy behind a breakwater

This experiment is to simulate a horizontal eddy behind a breakwater. The open channel configuration used in this experiment is 1500 m long, 300 m wide and 5 m deep. A breakwater is situated at $x = 300$ m with length of 150 m (see Figure 12). The water body is divided into 90 elements and 409 nodes in each of 11 layers. The open boundary conditions are set as the water levels of ± 5 mm at the inflow and -5 mm

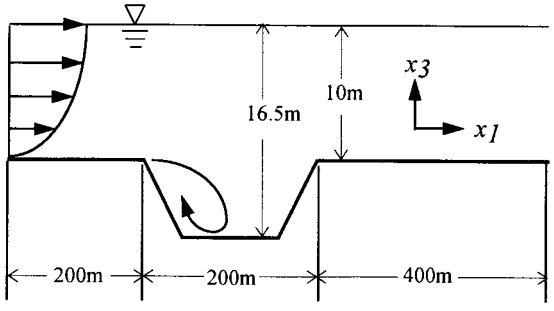

Figure 9. Geometry of the vertical recirculation experiment in a dredged channel on x_1–x_3 plane.

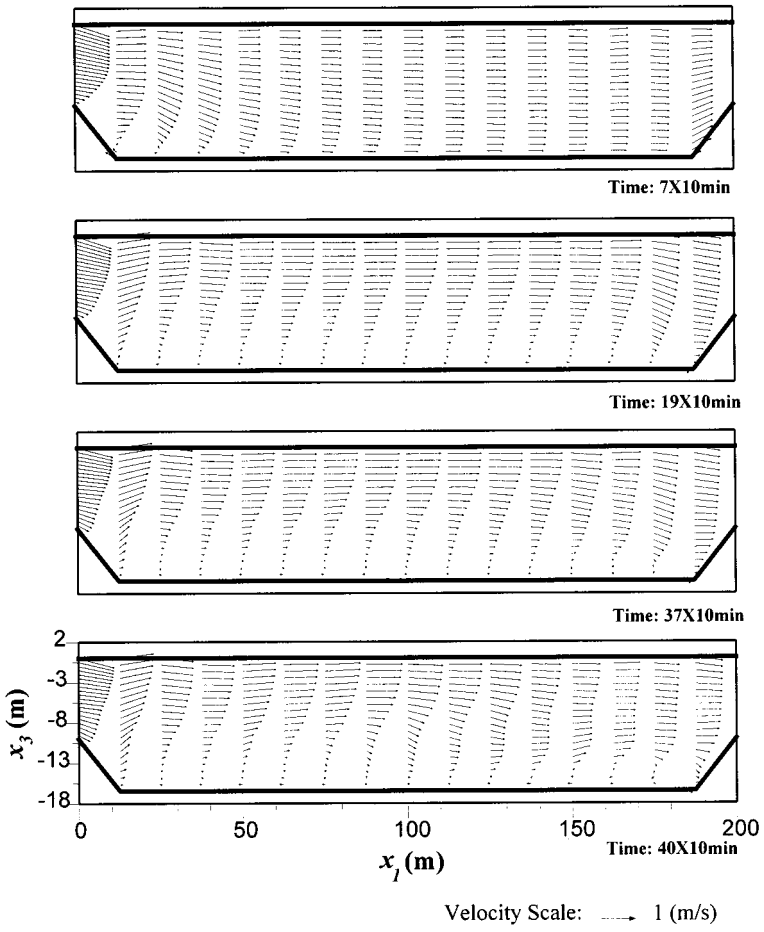

Figure 10. Initial development of vertical recirculations in a dredged channel.

at the outflow. The flow parameters employed here are the same as the previous numerical experiment in Section 6.3.

The development of an eddy behind the breakwater is clearly revealed in Figure 13. The eddy initially appears behind the breakwater and then expands and moves downstream. The numerical results reveal the true physical process of this type of flow.

7. CONCLUSIONS

The efficient and unconditional stable operator splitting method making use of the combined FEM and FDM has been established. Preinversing the coefficient matrix for the horizontal diffusion computations and employing FDM for vertical diffusion terms makes the present scheme highly efficient. The scheme is unconditionally stable because the implicit Eulerian–Lagrangian method for advection and implicit schemes for other terms are used. The nine isoparameteric shape function is employed for velocity, therefore, the scheme is of second-order-accurate in space. Furthermore, the algorithms are easily transformed to parallel computa-

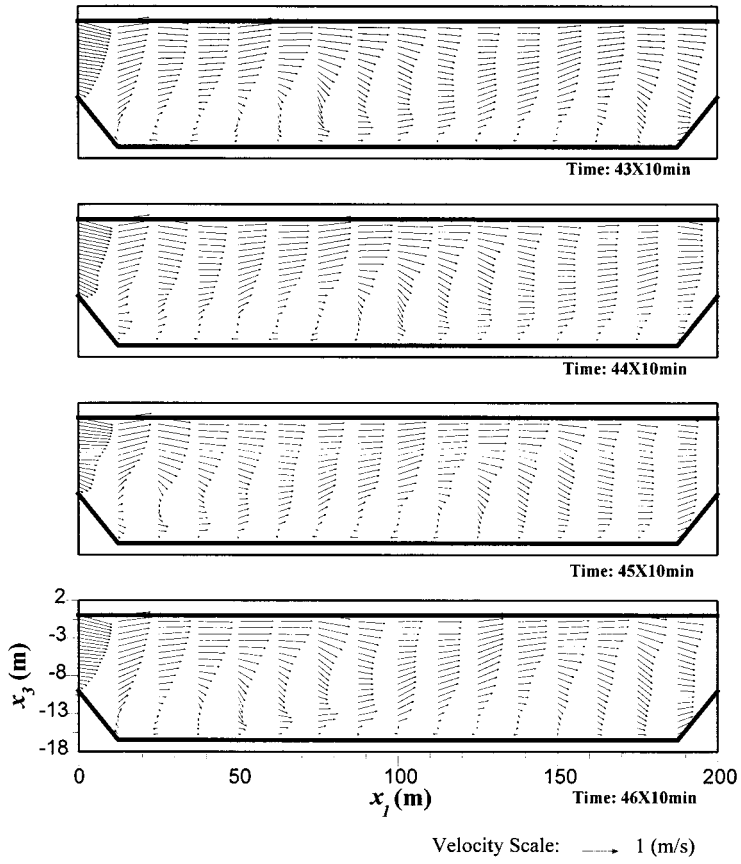

Figure 11. Alternate development of two vertical recirculations in a dredged channel.

tions. To investigate the applicability of the present method, a number of various numerical experiments have been performed. The computed results agree well with the analytical solutions and the other documented numerical solutions. The development of recirculations in a dredged ditch and behind a breakwater are consistent with real physical phenomena. This method is efficient and is tailored for complicated shallow water flow simulations.

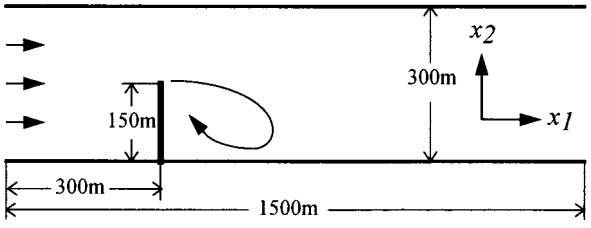

Figure 12. Geometry of a flow experiment past a breakwater in x_1–x_2 plane.

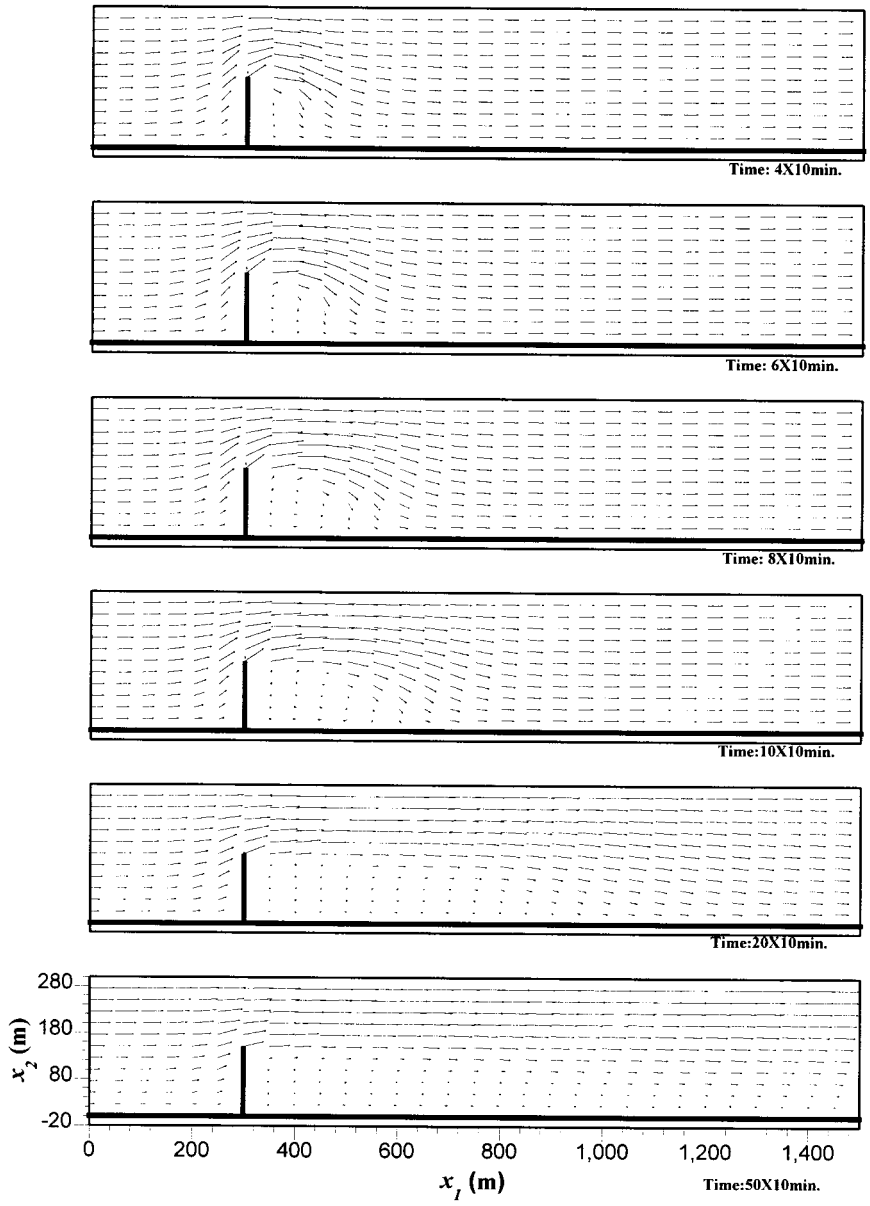

Figure 13. Development of an eddy behind a breakwater in the surface layer.

REFERENCES

1. S.R. Signorimi, 'A three-dimensional numerical model of circulation and diffusion-advection processes for estuarine and coastal application by finite element method', in T. Kawai (ed.), *Finite Element Flow Analysis*, University of Tokyo Press, Tokyo, 1982, pp. 603–610.
2. M. Kawahara, M. Kobayashi and K. Nakata, 'A three dimensional multiple level finite element method considering variable water density', in R.H. Gallagher, D.H. Norrie, J.T. Oden and O.C. Zienkiewicz (eds.), *Finite Element in Fluids*, Vol. 4, Wiley, Chichester, 1982, pp. 129–156.
3. Y.S. Li and J.M. Zhan, 'An efficient three-dimensional semi-implicit finite element scheme for simulation of free surface flows', *Int. j numer. methods fluids*, **16**, 187–198 (1993).

4. J.P. Benque, J.A. Cunge, J. Feuillet, A. Hanguel and F.M. Holly, 'New method of tidal current computations', *J. Waterway, Port, Coastal Ocean Div. ASCE*, **108**, 396–417 (1982).
5. J. Nicholson and B.A. O'Connor, 'Cohesive sediment transport model', *J. Hydraulic Eng ASCE*, **112**, 621–640 (1986).
6. P. Wilders, Th.L. van Stijn, G.S. Stelling and G.A. Fokkema, 'A fully implicit splitting method for accurate tidal computations', *Int. j. numer. methods eng.*, **26**, 2707–2721 (1988).
7. E.D. De Goede, 'A time-splitting method for the three-dimensional shallow water equations', *Int. j. numer. methods fluids*, **13**, 519–534 (1991).
8. J.J. Leendertse, 'Aspects of a computational model for long period water wave propagation', *Memorandum RM-5294-PR*, Rand, Santa Monica, CA, 1967.
9. T.J. Weare, 'Errors arising from irregular boundaries in ADI solutions of the shallow water equations', *Int. j. numer. methods eng*, **14**, 921–931 (1979).
10. V. Casulli, 'Semi-implicit finite difference methods for the two-dimensional shallow water equations', *J. Comput. Phys.* **86**, 56–74 (1990).
11. V. Casulli and R.T. Cheng, 'Semi-implicit finite difference methods for three-dimensional shallow water flow', *Int. j. numer. methods fluids*, **15**, 629–648 (1992).
12. F. Thomasset, *Implementation of Finite Element Methods for Navier–Stokes Equation*, Springer, New York, 1981.
13. R. Glowwinski and O. Pironneau, 'On a mixed finite element approximation of Stokes problem', *Numerische Mathematik*, **33**, 397–424 (1979).
14. A.M. Davies and A. Owen, 'Three dimensional numerical sea model using the Galerkin method with a polynomial basis set', *Appl. Math. Model.*, **3**, 421–428 (1979).
15. G. Gomini, M. Manzan and C. Nonino, 'Analysis of finite element schemes for convection-type problems', *Int. j. numer. methods fluids*, **20**, 443–458 (1995).
16. C. Koutitas and B. O'Connor, 'Modeling three-dimensional wind-induced flows', *J. Hydraul. Div., ASCE*, **106**, 1843–1865 (1980).

